Inorganic Chemistry Communications 159 (2024) 111816

Contents lists available at ScienceDirect

Inorganic Chemistry Communications

journal homepage: www.elsevier.com/locate/inoche

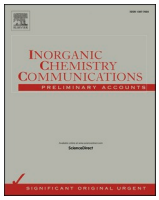

Short communication

The outstanding electrochemical performance of porous hexagonal boron nitride as a K-ion battery anode

Nelly Esther Flores Tapia [a,**], Vanessa Valverde [b], Gabriel Moreano [b], Subhash Chandra [c,*], Luis Buenaño [b], Ahmad Ismael Saber [d], Hala Bahair [e], Parminder Singh [f], Yasser Elmasry [g]

[a] Research and Development Directorate, Faculty of Sciences, Food and Biotechnology, Technical University of Ambato, Ambato, Ecuador
[b] Facultad de Mecánica, Escuela Superior Politécnica de Chimborazo (ESPOCH), Panamericana Sur km. 1 1/2, Riobamba, 060155, Ecuador.
[c] Department of Electrical Engineering, GLA University, Mathura 281406, India
[d] Department of Dentistry, Al-Noor University College, Nineveh, Iraq
[e] Medical Technical College, Al-Farahidi University, Iraq
[f] Chemical Engineering Department, Thapar Institute of Engineering and Technology, Patiala, India
[g] Department of Mathematics, Faculty of Science, King Khalid University, P.O. Box 9004, Abha 61466, Saudi Arabia

ARTICLE INFO

Keywords:
Hexagonal boron nitride
Theoretical specific capacity
K-ion
Porosity
Storage process

ABSTRACT

Within the current piece of research, we propose a porous model of hexagonal boron nitride (h-BN) monolayer (h-BNML) through DFT calculations in order develop an anode material for KIBs. We in particular focused on the impact of the pore on the diffusion of K ions and upon the storage process. We created the porous model of the h-BNML by using a pure h-BNML structure via the removal of B atoms which mimics the formation of the pore. Based on the DFT calculations, there was no change in the original planar structure of the h-BNML after the formation of the pore. There was a dramatic change in the electronic and structural attributes of the h-BNML indie the poor based on the introduced vacancies, which allowed the K-ion to adhere effectively within the pore. Based calculations demonstrated the interaction between the K ions and the pores through electrostatic attraction. The model exhibited the ability to keep a high number of K ions at its surface without any change in the initial planar structure of h-BN, which was closely associated with an increased theoretical specific capacity, which increased with porosity. Hence, the pore formation increased the diffusion of K ions in comparison with the pure h-BNML. This can be insightful to designing enhanced anode materials for KIBs. Finally, the current work can provide insights into tailoring porous BN materials for application in KIBs.

1. Introduction

Recent years have witnessed the application of electrochemical devices, including rechargeable batteries, in energy storage devices, electric vehicles, transportable power devices as well as electronic accessories [1–5]. Metal-ion batteries (MIBs) in particular have enjoyed considerable global interest thanks to their long cycle life, superior power as well as high specific energy [6–10] . As an instance, recent years have witnessed an increase in the application of KIBs, SIBs, and LIBs [11–14] . However, one of the main drawbacks to KIBs is to find electrodes with high energy density [15–19]. Researchers have investigated numerous materials to overcome the drawback mentioned above and to understand the performance of current electrodes at the atomic level [20].

Recently carried out studies into two-dimensional (2D) carbon nanostructures (CNSs) have found that they have unique characteristics, which can be utilized as an anode material in the future KIBs, SIBs and LIBs [21–30]. CNSs can be conducive to designing new 2D systems that could be utilized as an anode material in MIBs. As an example, in a study by Xu et al. [31], a porous carbon material was synthesized to be used as an anode material in KIBs using inter-connected pores and edged-doped atoms around the pores. After 200 cycles at 0.1 Ag^{-1}, the battery capacity reached 409 $mAhg^{-1}$. The DFT computations demonstrated that the edge-doped atoms led to an increase in the sorption of K ions, thereby enhancing the capacity. Furthermore, the electric field responsive switch was employed to anchor polysulfides on porous carbon

* Corresponding author.
** Co-corresponding author.
E-mail address: ne.flores@uta.edu.ec (N.E.F. Tapia).

https://doi.org/10.1016/j.inoche.2023.111816
Received 14 September 2023; Received in revised form 15 November 2023; Accepted 26 November 2023
Available online 29 November 2023

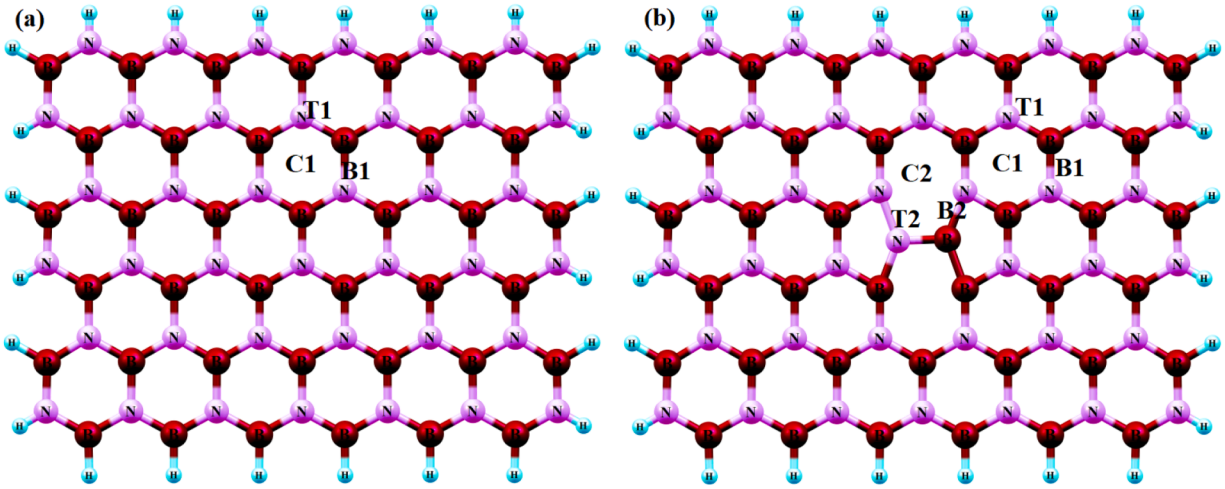

Fig. 1. The relaxed configurations of the two types of BN monolayers examined, namely, the (a) unmodified h-BN (pristine) and (b) h-BN with a pore (pore h-BN).

aerogels in Li/S batteries to improve their capacity, which increased at 0.2C to 1307 $mAhg^{-1}$ and kept eighty-four percent of the initial capacity following hundred cycles [32]. A theoretical/experimental study was carried out by Chen et al. [33] into P-doped porous C for zinc-air batteries. The density functional theory computations were undertaken to investigate the separate flakes of graphene (Gr) layers, where C atoms were replaced with the P atoms at the edge and inner sides of Gr. The results demonstrated the doping the P atoms at the edge of the pores were conducive to improving the bi-functional catalytic activity that affected the performance of Zn-air batteries. Zhao et al. [34] theoretically and experimentally investigated the application of N-doped porous C as an anode material in KIBs [35–37]. By retaining its stability after hindered cycles at 0.74 Ag^{-1}, battery discharge specific capacity reached 113 $mAhg^{-1}$. DFT calculations were done on the formation of at a periodic Gr model where K ions were adhered.

By reviewing the studies mentioned above, we can conclude that introducing heteroatoms and the presence of pores lead to a rise in the interaction between the surface of cathodes and metal ions, which can raise the capacity of batteries. Similarly, introducing defected vacancies such boron nitride (BN) in a structure with various atoms can be a b = vial method to design high-performance electrodes. The hexagonal boron nitride (h-BN) monolayer (h-BNML) is a thin material which has nitrogen (N) and boron (B) atoms and its stoichiometry is 1:1. These B and N atoms have been arranged in a sp^2-bonded honeycomb lattice. The monolayer is isoelectronic and isostructural to Gr [38], where N and B frame the C atoms in periodic table, which feature 8 valence electrons for every BN which involve in a weaker π bonds and robust in-plane σ bonds. In comparison with C-based relatives, 2D h-BN monolayers consist of bulk-like h-BN, which has a layered structure similar to Gr [39–43].

The results obtained based on theoretical computations have been tested experimentally, where porous h-BN models have been used as an anode material. However, no studies have investigated the key role of pores in mechanisms that result in an increased energy storage. In addition, no previous study has investigated parameters like open circuit voltage (OCV) and specific capacity (SC) at the DFT level for porous h-BNMLs. The current study aims at investigating the role of pore size in retaining and diffusing K ions over the interface of porous h-BNMLs. Also, the current study intends to achieve robust parameters for easily fabricating porous h-BNs with improved structural and electronic characteristics. The methodological procedures used in this study could pave the way for designing h-BNMLs for usage as an anode material in KIBs.

2. Methodological details

We utilized the basis set 6-31G (d) and the functional B3LYP for performing the electronic analyses, structural optimizations and energy computations. To accurately predict the weak interactions, the "D3" term was included [44]. B3LYP can be used to investigate the structural and electronic characteristics of many nano-materials [45–49]. The computations were all done using the GAMESS software [50]. The Bader charge analysis was performed to investigate the amount of charge transport between the h-BNML and the K ions [51]. Also, we investigated the paths for diffusion of K ions, and the NEB method [52] was used to calculate diffusion barrier energy [52]. Furthermore, the - adhesion energy of the K atoms onto the h-BNML was computed as follows [53]:

$$E_{ad} = \frac{(E_{K@h-BN} - (E_{h-BN} + xE_K))}{x} + E_{BSSE} \quad (1)$$

where we simplify the charge/discharge processes of h-BNMLs as the half-cell reactions as follows:

$$xK^+ + xe^- + h - BN \rightleftharpoons K_x@h - BN \quad (2)$$

Based on the reaction model above, the open-circuit voltage (V_{OCV}) was estimated as below [53]:

$$V_{OCV} = \frac{(E_{K@h-BN} - (E_{h-BN} + xE_K))}{xe} \quad (3)$$

where x is the number of K ions, E_K represents energy of a K atom in the bulk systems, $E_{h\text{-}BN}$ represents the energy of the pure h-BNML and $E_{K@h\text{-}BN}$ represents the total energy of K atoms adhered on the h-BNML. A negative value of adhesion energy shows the adhesion of K atoms onto the pure h-BNML. The maximum storage capacity (C) was computed using Eq. (4) [54–56]:

$$C = \frac{x_{max}F}{M} \quad (4)$$

here, F represents the Faraday's constant (26.801 A h mol^{-1}), x_{max} designates the number of K atoms adsorbed at the maximum adhesion concentrations and M represents the atomic mass. The charge transport analysis of the K ions to modified BNMLs was performed to characterize the electronic density distributions through the 3D isosurfaces of charge density difference $\Delta\rho$.

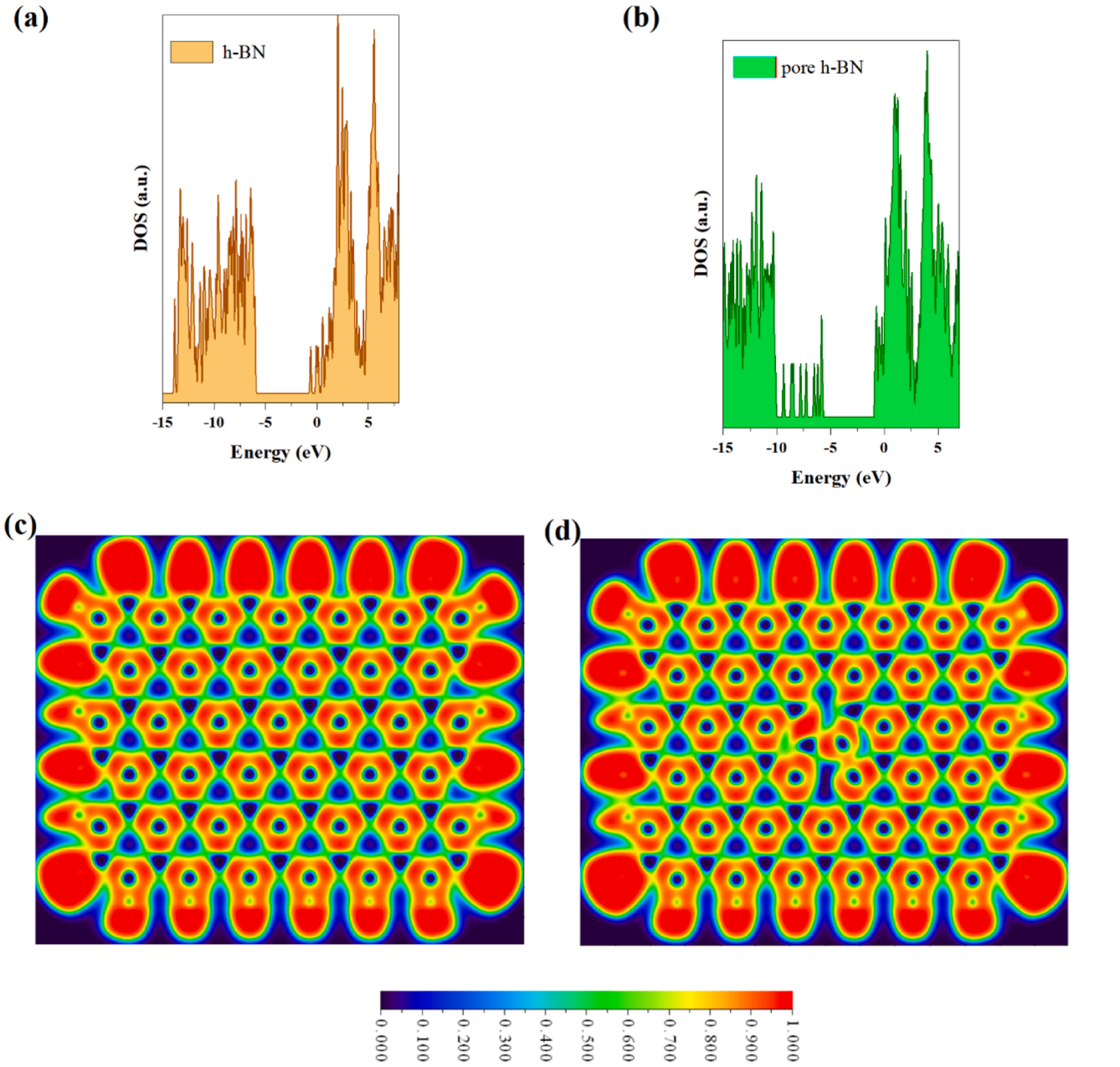

Fig. 2. The density of states plots for both types of BN monolayers examined, namely, (a) pristine h-BN and (b) pore h-BN. Additionally, contour plots of the ELF map are presented for these systems, where the values range from 0.0 to 1.0. A value of 1 (in red) indicates complete electron localization, while a value of 0 (in blue) signifies the absence of electron distribution. (For interpretation of the references to colour in this figure legend, the reader is referred to the web version of this article.)

3. Results and discussions

3.1. Geometrical descriptions and electronic/structural attributes of porous h-BNMls

Fig. 1 (a) illustrates the geometrical structure of the pure h-BnML. After geometrical relaxation, the original 6-ring structure in the h-BNMl was disrupted. The computations demonstrated that the lattice parameter of the h-BNMl was 6.89 Å, similar to the value obtained in the literature [57]. The bandgap of the pure h-BNML was approximately 5.23 eV, similar to the value obtained in the literature [58]. This shows the reliability and accuracy of the method employed within the current work, so it can accurately describe the electronic structure of h-BNMl. Single B (V_B) or N (V_N) vacancies must be created in the h-BNML first for creating a porous h-BNML. We considered several possible configurations for this type of defect. The calculated defect formation energy (E_{def}) for this configuration was found to be the most stable compared to other configurations. The geometries of the defected h-BNML with most stability is shown in Fig. 1 (b). In both defects, the BNMl retailed its planarity. Based on the results, the V_B in the h-BNML was more favorable than the V_N in terms of energy, which could be ascribed to the to the presence of repulsion between the dangling N atoms, which prevented the unstable N-N bonds to be formed. We should mention that, in spite of the presence of di-vacancies defect (di-DV) found in previous DFT studies [59], there was no di-vacancy (V_{BN}) in the current study. Furthermore, the configurations achieved for the vacancies were consistent with the lower energy formation geometries derived from previous DFT investigations [60]. In addition, a distinct spin-splitting

Table 1
Partial Bader charges (Q), and adhesion energies (E_{ads}) of the K ions adhered on the h-BNMLs.

Monolayers	Site	E_{ads} (eV)	Q (e)
h-BN	C1	−1.23	0.726
	T1	−0.94	0.403
	B1	−1.05	0.551
	C2	–	
	T2	–	
	B2	–	
Pore h-BN	C1	−2.27	0.672
	T1	−1.87	0.599
	B1	−1.94	0.523
	C2	−3.69	0.864
	T2	−3.62	0.812
	B2	−3.64	0.855

with distinct defect levels was detected in the bandgap region (4.57 eV) through the analysis of the density of states (DOS) for the VD. In the V_B, the existence of a B vacancy defect led to a magnetic moment of around 3 μ_B. Also, right after the formation of the B vacancy in h-BNML, 1 spin-up and 2 spin-down occupied states appeared above the Fermi level (see the DOS plot in Fig. 2a-b). These donor states mainly consisted of of N-2p states and they were localized onto the dangling N atoms near the defect region. There was a great electronic de-localization at the B and N atoms near the pore due to the pore size, which was evident based on the electron localization function (ELF) in two-dimensional diagrams (Fig. 2 (a-b)). It should be noted that the ELF value of 1.0 indicated perfect localization and the value of 0.0 indicated the lack of electron density, whereas the value of 0.5 indicated the presence of a metallic bond [61]. Based on the the $E_{cohesive}$ value (-10.39 eV/atoms), the defected h-BNML exhibited a negative value in the h-BNML.

3.2. *The adhesion of K ions and the electronic/structural attributes of porous h-BNML*

According to the geometrical configuration due to the pore, identifying 3 various symmetry points was possible, namely T, B and C, which represent the top site over B or N atoms, a bridge site between B-N atoms

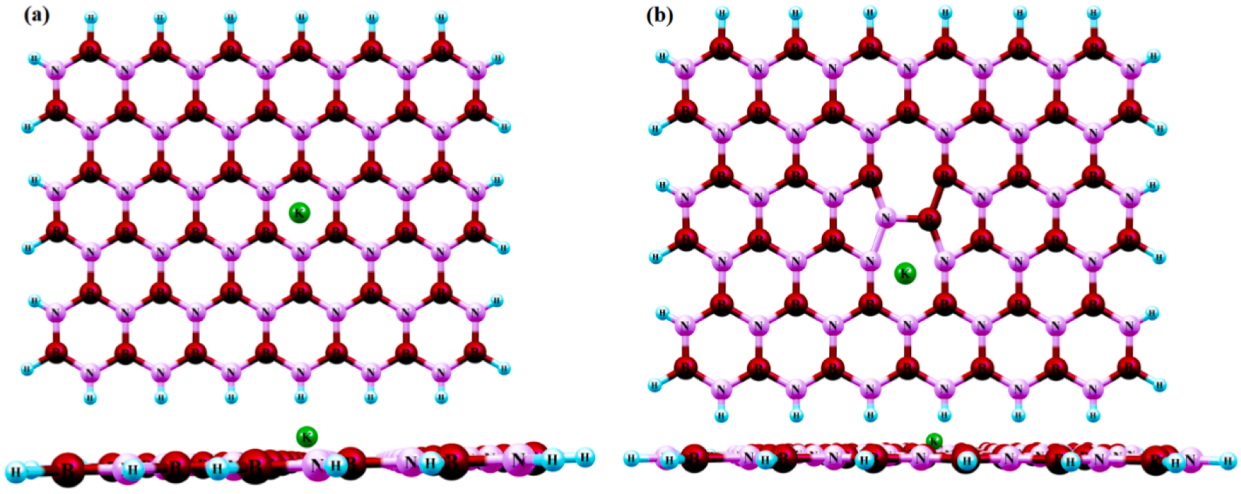

Fig. 3. Most stable configuration of the K-ion adsorption on the BNMLs: (a) h-BN-K, (b) pore h-BN-K.

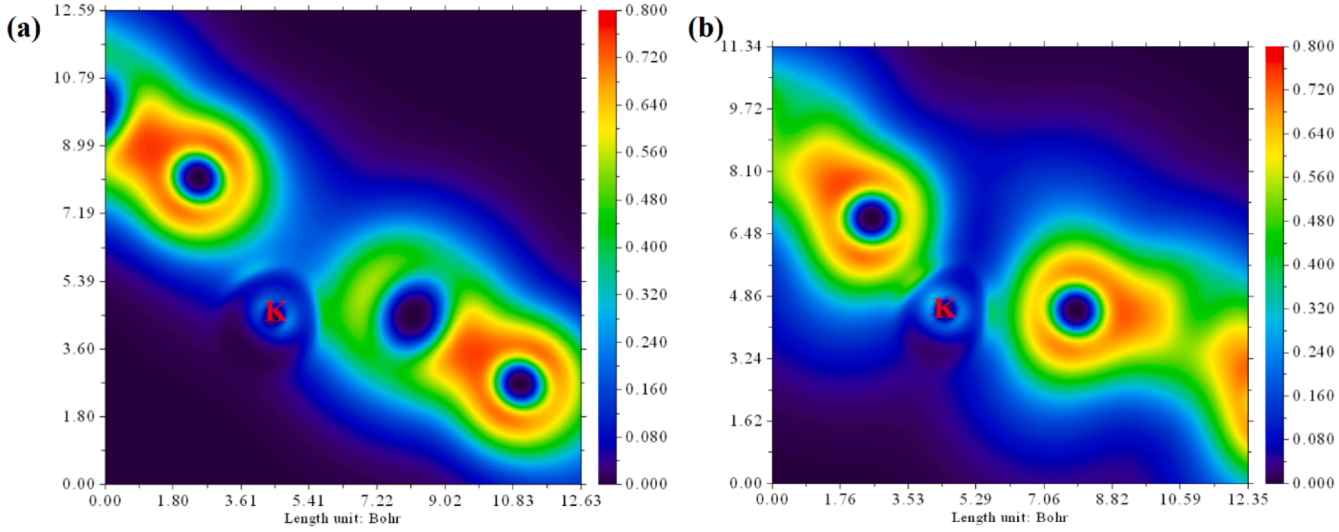

Fig. 4. Illustrates the interactions between k ions and bnmls through isosurfaces of charge density differences and 2d slices. Specifically, we can observe these interactions in the systems (a) h-bn-k and (b) pore h-bn-k.

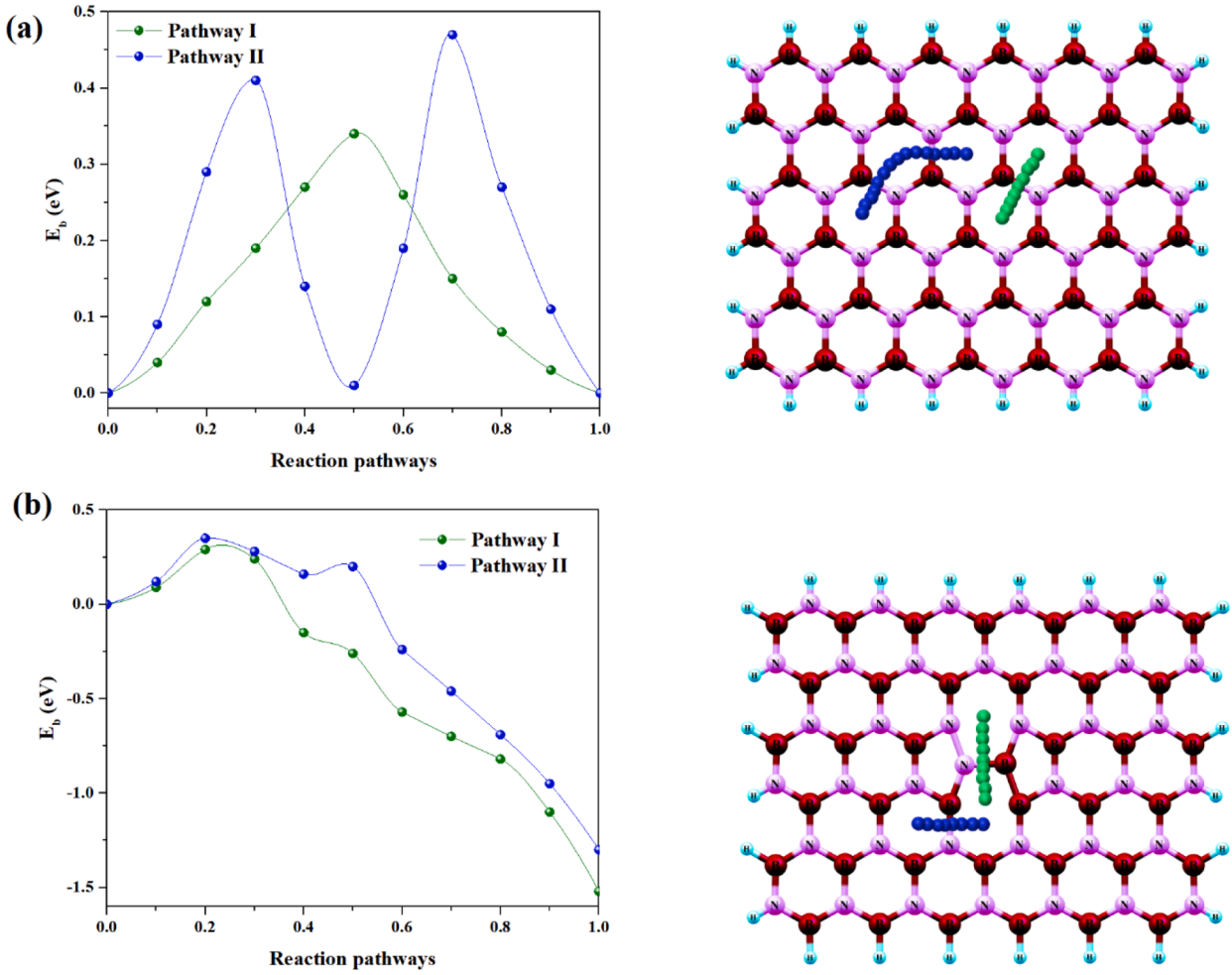

Fig. 5. Two possible diffusion paths (green and blue lines) of the K ions on the BNMLs: (a) h-BN-K, (b) pore h-BN-K. (For interpretation of the references to colour in this figure legend, the reader is referred to the web version of this article.)

for B and a hollow site at the centre of the pore ring for C respectively. As shown in Fig. 1b, we set up some groups of such symmetry sites shown by pink labels. These sites were employed for allowing the interaction of K ions of the pore h-BN matrices. The K atom was repositioned at the symmetry sites shown in Fig. 1b to perform the interactions of the K ions with the BN matrix of the pore. As revealed by the charge analysis mentioned below, the K atom was finally changed to an ion, Table 1 lists the adhesion energy for each site. The adhesion energy of the pure h-BNML was similar and the highest energy was found at C1, which could be sue to the electron de-localization near C1 (see Fig. 1(c)). The K ion was more likely to be adhered because of its behaviour because the electron de-localization reduced at site T1 and site B1.

The adhesion energy of the porous h-BNML with 1B atom vacancy was − 3.69 eV, which was probably because of the fact that the formed pore was symmetric, and because of the fact that the electron de-localization enlarged (see Fig. 2(d)). The symmetric breaking of the ELF surrounding B1 due to the rise in the electron delocalization at this site (Fig. 2(d)) could also be the reason for such a behaviour. There was almost no change in the ELF values at C1 and T1 and there was no strengthening in the adhesion (see Table 1). The results of Bader charge analysis can be d = found Table 1 for each o K ion that had an interaction with the pure h-BNML. The values were in the range of + 0.726 to + 0.864, which demonstrated that a K cation was formed in each system. In addition, the geometries of the sites are shown in Fig. 3, where the K-ion was introduced with the ultimate configurations with most stability.

Fig. 4 (a–b) shows the adhesion of K-ion on the pure h-BNML with interaction energy which is probably a van der Waals interaction. It may be due to the magnitude of the attraction and separation to the mono-layer plane, and it could be related to an alloying-conversion interaction that would rule the energy storage mechanism in a porous BN anode of a K-ion battery.

We also map the density difference isosurfaces in 3D arrangements to further investigate the interaction between the K ions and BNML (see Fig. 4(a-b)). For each item, the insets displayed 2D sections of the charge density difference ($\Delta\rho$) at a perpendicular of h-BNML. The red-colored areas demonstrated areas where there was an excess of electron formation due to the charge transport between the h-BNML and the K ions. The formation of excess electrons was located mainly at the interfaces between the K ions and the h-BNML matrix for the and porous and pure models (see Fig. 4 (a-b)). However, as illustrated in Fig. 4(b), the pore model had a different behaviour, i.e., the electron excess was almost around the pore, which was shown by the slices at the plane of the h-BNML matrix.

3.3. K Ion diffusion

The diffusion paths through which the K ions were allowed to travel on the BNML were investigated to further understand the performance of the h-BNML. The CI-NEB method, which is an accurate method to calculate the activation barrier, was used to investigate the paths. The

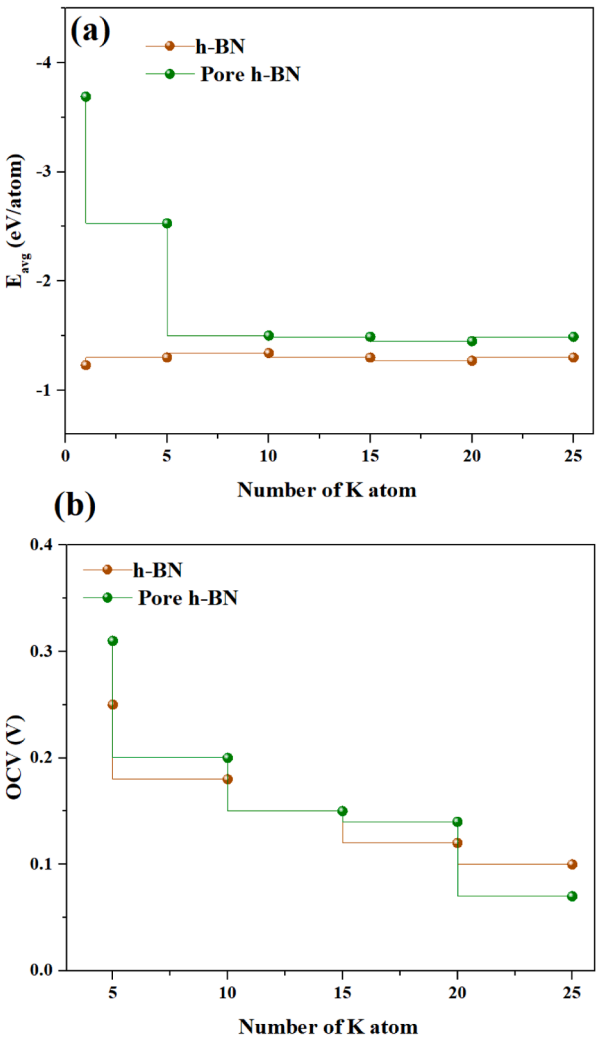

Fig. 6. Average adsorption energy (e_{avg}) values and (b) computed OCV for all adhered K ions.

NEB method can be used to accurately compute the saddle points [62]. The main criterion for selecting the pathway for energy penetration is the energy barrier along that pathway. Given the symmetry of the perfect and defective structures, other pathways for penetration can also be considered. We also considered all of them. However, only the two pathways with the lowest energy barriers are reported. Two potential paths were identified to allow the K ions to migrate on the h-BNML matrix (see Fig. 5a). For the modified h-BNMLs, the configuration with the lowest energy was considered the ultimate step for the diffusion of K-ions. The diffusion path 1 for h-BNML exhibited an easy path through which the K ions migrated easily because of the fact the energy barrier was small (0.35 eV). However, diffusion path 2 exhibited a large value, which showed that the activation energy remained the same despite the fact the path seemed to need larger energy because of the trajectory bending. As shown in Fig. 5, we also tested the diffusion paths for the pore model. The energy barriers for penetration in the defected structure in pathways 1 and 2 are respectively 0.23 and 0.26 eV, which are both lower than the energy barrier for penetration in the perfect structure. Both paths exhibited an energy barrier which was smaller than that of other 2D materials [63–65]. The ELF contribution near the pore could be the reason for the reduction in the values. The de-localization of electrons might facilitate the transportation of ions at its interface. In the porous h-BNML, the suggested trajectories and the pore size revealed a greater quantity of transition states along the pathways, which was probably because of the migration of K ions that crossed the pore with less possibility compared to that in the pure h-BNML. As a result, the pore obviously improved the diffusion of K ions in comparison with the pure h-BNML.

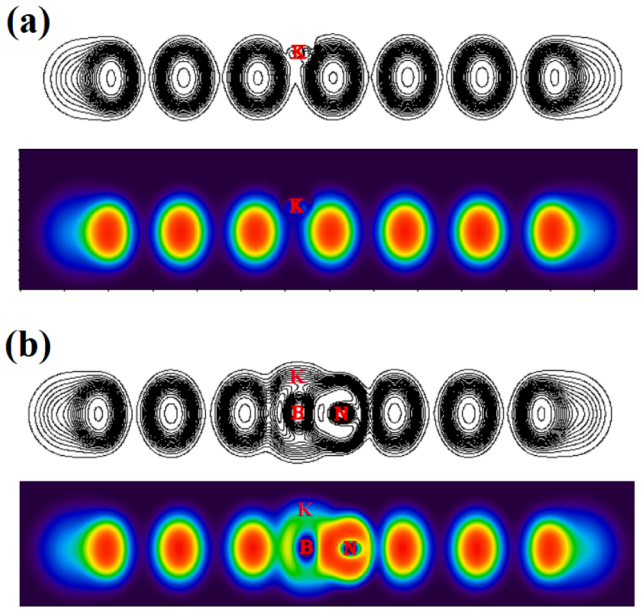

Fig. 7. Electronic localization function (ELF) for the K-ions adhered on the BNMls: (a) h-BN-K, (b) pore h-BN-K.

Table 2
TSC and OCV of the h-BNMLs that act as a two-dimensional anode.

Monolayers	n	Capacity ($mAhg^{-1}$)	OCV (V)
h-BN	5	187.11	0.25
	10	349.35	0.18
	15	577.95	0.15
	20	895.91	0.12
	25	1167.41	0.10
Pore h-BN	5	193.77	0.31
	10	363.39	0.20
	15	6.11.47	0.15
	20	916.51	0.14
	25	1218.79	0.07

3.4. OCV and storage capacity (SC)

The DFT calculations were performed to compute the OCV and SC, which are important parameters in developing anode materials for alkaline metal batteries. Equation (4) was used to the compute the adhesion energy of K ions to evaluate OCV and SC (see Fig. 6). i.e., the step graph compares the adhesion energy assessed after the adhesion of different number of K ions, namely 5, 10, 15, 20, and 25. The h-BNML in particular tended to keep E_{ads} (Fig. 6). This indicated that the pure h-BNML retained the K ions at constant adhesion energy lower than − 1.30 eV, which was probably due to the weak electrostatic interaction. The porous h-BNML exhibited E_{ads} below − 2.53 eV for the number equal 5, which reduced to − 1.49 eV when the concentration of K ions was higher. However, the interaction strength increased after many K ions was added (Fig. 6). This indicated the impact of the pore size upon the K ion retention ability of BN. The ELF method can be used to further understand this. The slices of the ELF plot at the interface of h-BNMLs and K ions are shown in Fig. 7, which showed the ionic nature of the

interaction. As shown in Fig. 2d, the ELF distribution can explain the adhesion mechanism. As shown in Fig. 2(d), a stronger adhesion energy can be expected because of the de-localization of electrons after the formation of the pore.

The relationship between the adhesion of K ions and the resulting OCV is depicted in Table 2 and Fig. 6b. There is a direct relationship between the OCV of materials and their collective capacity for producing a potential, which is due to the electron density upon the surface of BN. Also, there was an increase due to the existence of many K ions adhered on the surface, and not just due to a single ion, which changes potential energy, and causes the given potential. So, an average energy is required due to the presence of many K on the surfaces based on equation (3). We should mention that this definition was also expressed since volume and entropy were slight because of their unsubstantial amount [66]. The step plot revealed that h-BNML and the porous h-BNML showed OCV in the range of around 0.17 to 0.31 V, and pore model exhibited the largest value of 0.31 V, which was probably because of the amount of adhesion energy. After an increase in the number of adhered K ions ($n > 5$), the OCV values converged to a voltage interval of 0.31 to 0.07 V. Moreover, we calculated the OCV for the adhesion of K-ion from $n = 1$ to 25. These values can be considered enough for battery usage because they remained at a voltage required for portable devices, especially, bv values less than 0.1 V are related to high concentration of K ions [67].

Also, Equation (4) was used to compute the theoretical specific capacity (TSC). For comparing, we simulate the porous h-BNML the h-BNML with vacancies, and we subject the h-BNMLs to the adhesion of K ions onto their surface. The analysis was done with $n = 5$, 10, 15, 20, and 25 K ions. When the number of adhered K ions increased on the surface of the monolayer, its TSC increased (see Table 2). The TSC of the for porous h-BNML was higher compared to that of the pure h-BNML. When the number of K ions reached its maximum, the TSC increased by 4.02 % in comparison with the pure h-BNML. Additionally, the OCV values converged to similar values when larger TSCs were assessed.

4. Conclusions

The electronic and structural attributes related to the adhesion of K ions onto the porous h-BNML monolayers were investigated systematically through the DFT-D3 level of theory. Other experimented research studies can be performed and enlightened using the procedures within the current study. Also, new two-dimensional materials can be tailored for energy storage purposes. Based on the results, there was no change in the planar structure of the porous h-BNML after the BN vacancies were formed. There was a dramatic changed in the electronic structure of porous h-BNML after the formation of the pores, which resulted in an increased electron delocalization, which was evident based on the calculation of the ELF parameters at these sites. We also assessed the adhesion of K ions in the pore regions and symmetry regions near the pore. Obviously, the existence of pore affected the redistribution of the electron density following the adhesion of K ions, which also facilitated its maintenance at the pore region. There was a tremendous adhesion of K ions on the porous h-BNML, which demonstrated the impact of the pore on the adsorption of many K on the pore structure. The possible pathways which K ions could follow were evaluated to investigated the diffusion of the K ions. There was an increase in the diffusion of K ions in the reverse direction of mobility because of the pore in the porous h-BNML, which was probably due to the particular range where the pore distribution has a direct effect on the energy storage attributes. We can address this to improve the properties of porous h-BNML, which facilitates ion mobility.

Declaration of competing interest

The authors declare that they have no known competing financial interests or personal relationships that could have appeared to influence the work reported in this paper.

Data availability

No data was used for the research described in the article.

Acknowledgments

The authors extend their appreciation to the Deanship of Scientific Research at King Khalid University for funding this work through the Large Groups under grant number (RGP.2/582/44).

References

[1] L.B. Diaz, X. He, Z. Hu, F. Restuccia, M. Marinescu, J.V. Barreras, Y. Patel, G. Offer, G. Rein, Meta-review of fire safety of lithium-ion batteries: Industry challenges and research contributions, J. Electrochem. Soc. 167 (2020), 090559.
[2] M.S. Dresselhaus, I. Thomas, Alternative energy technologies, Nature 414 (2001) 332–337.
[3] S. Wang, S. Zhao, X. Guo, G. Wang, 2D material-based heterostructures for rechargeable batteries, Adv. Energy Mater. 12 (2022) 2100864.
[4] W. Hao, J. Xie, Reducing diffusion-induced stress of bilayer electrode system by introducing pre-strain in lithium-ion battery, J. Electrochem. Energy Convers. Storage 18 (2021), 020909.
[5] C. Lu, H. Zhou, L. Li, A. Yang, C. Xu, Z. Ou, J. Wang, X. Wang, F. Tian, Split-core magnetoelectric current sensor and wireless current measurement application, Measurement 188 (2022), 110527.
[6] X. Zhang, Y. Tang, F. Zhang, C.S. Lee, A novel aluminum–graphite dual-ion battery, Adv. Energy Mater. 6 (2016) 1502588.
[7] K. Abraham, How comparable are sodium-ion batteries to lithium-ion counterparts? ACS Energy Lett. 5 (2020) 3544–3547.
[8] X. Tong, F. Zhang, B. Ji, M. Sheng, Y. Tang, Carbon-coated porous aluminum foil anode for high-rate, long-term cycling stability, and high energy density dual-ion batteries, Adv. Mater. 28 (2016) 9979–9985.
[9] S. Mu, Q. Liu, P. Kidkhunthod, X. Zhou, W. Wang, Y. Tang, Molecular grafting towards high-fraction active nanodots implanted in N-doped carbon for sodium dual-ion batteries, Natl. Sci. Rev. 8 (7) (2020).
[10] S. Li, J. Chen, X. He, Y. Zheng, C. Yu, H. Lu, Comparative study of the micro-mechanism of charge redistribution at metal-semiconductor and semimetal-semiconductor interfaces: Pt (Ni)-MoS2 and Bi-MoS2 (WSe2) as the prototype, Appl. Surf. Sci. 623 (2023), 157036.
[11] C. Qiu, L. Jiang, Y. Gao, L. Sheng, Effects of Oxygen-Containing Functional Groups on Carbon Materials in Supercapacitors: A Review, Mater. Des. 111952 (2023).
[12] W. Li, X.-S. Chu, F. Wang, Y.-Y. Dang, X.-Y. Liu, X.-C. Wang, C.-Y. Wang, Enhanced cocatalyst-support interaction and promoted electron transfer of 3D porous g-C3N4/GO-M (Au, Pd, Pt) composite catalysts for hydrogen evolution, Appl Catal B 288 (2021), 120034.
[13] C. Wang, H. Shang, J. Li, Y. Wang, H. Xu, C. Wang, J. Guo, Y. Du, Ultralow Ru doping induced interface engineering in MOF derived ruthenium-cobalt oxide hollow nanobox for efficient water oxidation electrocatalysis, Chem. Eng. J. 420 (2021), 129805.
[14] Q. Li, H. Wang, H. Yu, M. Fu, W. Liu, Q. Zhao, S. Huang, L. Zhou, W. Wei, X. Ji, Engineering an Ultrathin and Hydrophobic Composite Zinc Anode with 24 μm Thickness for High-Performance Zn Batteries, Adv. Funct. Mater. 2303466 (2023).
[15] M. Wang, C. Jiang, S. Zhang, X. Song, Y. Tang, H.-M. Cheng, Reversible calcium alloying enables a practical room-temperature rechargeable calcium-ion battery with a high discharge voltage, Nat. Chem. 10 (2018) 667–672.
[16] Y. Dou, A. Wang, L. Zhao, X. Yang, Q. Wang, M.S. Sudi, W. Zhu, D. Shang, Boosted hydrogen evolution reaction for a nitrogen-rich azo-bridged metallated porphyrin network, J. Colloid Interface Sci. 650 (2023) 943–950.
[17] X. Chen, S. Lv, J. Kang, Z. Wang, T. Guo, Y. Wang, G. Teobaldi, L.-M. Liu, L. Guo, Efficient C-N coupling in the direct synthesis of urea from CO2 and N2 by amorphous SbxBi1-xOy clusters, Proc. Natl. Acad. Sci. 120 (2023) e2306841120.
[18] W. Liu, Q. Zhao, H. Yu, H. Wang, S. Huang, L. Zhou, W. Wei, Q. Zhang, X. Ji, Y. Chen, Metallic Particles-Induced Surface Reconstruction Enabling Highly Durable Zinc Metal Anode, Adv. Funct. Mater. 2302661 (2023).
[19] H. Yu, D. Chen, X. Ni, P. Qing, C. Yan, W. Wei, J. Ma, X. Ji, Y. Chen, L. Chen, Reversible adsorption with oriented arrangement of a zwitterionic additive stabilizes electrodes for ultralong-life Zn-ion batteries, Energ. Environ. Sci. (2023).
[20] J. Xu, Y. Dou, Z. Wei, J. Ma, Y. Deng, Y. Li, H. Liu, S. Dou, Recent progress in graphite intercalation compounds for rechargeable metal (Li, Na, K, Al)-ion batteries, Adv. Sci. 4 (2017) 1700146.
[21] R.P. Joshi, B. Ozdemir, V. Barone, J.E. Peralta, Hexagonal BC3: A robust electrode material for Li, Na, and K ion batteries, The Journal of Physical Chemistry Letters 6 (2015) 2728–2732.
[22] S. Yang, S. Li, S. Tang, W. Dong, W. Sun, D. Shen, M. Wang, Sodium adsorption and intercalation in bilayer graphene from density functional theory calculations, Theor. Chem. Acc. 135 (2016) 1–11.
[23] K.C. Wasalathilake, G.A. Ayoko, C. Yan, Effects of heteroatom doping on the performance of graphene in sodium-ion batteries: A density functional theory investigation, Carbon 140 (2018) 276–285.
[24] N. Dimakis, I. Salas, L. Gonzalez, O. Vadodaria, K. Ruiz, M.I. Bhatti, Li and Na adsorption on graphene and graphene oxide examined by density functional

theory, quantum theory of atoms in molecules, and electron localization function, Molecules 24 (2019) 754.
[25] F. Wang, H. Zhao, J. Liang, T. Li, Y. Luo, S. Lu, X. Shi, B. Zheng, J. Du, X. Sun, Magnetron sputtering enabled synthesis of nanostructured materials for electrochemical energy storage, J. Mater. Chem. A 8 (2020) 20260–20285.
[26] O.A. Jaramillo-Quintero, R.V. Barrera-Peralta, A.G. El Hachimi, A. Guillén-López, O. Pérez, E. Reguera, M.E. Rincón, J. Muñiz, Understanding the interaction between heteroatom-doped carbon matrix and Sb2S3 for efficient sodium-ion battery anodes, J. Colloid Interface Sci. 585 (2021) 649–659.
[27] A.G. El Hachimi, A. Guillén-López, O.A. Jaramillo-Quintero, M.E. Rincon, P. Y. Sevilla-Camacho, J. Muniz, Exploring the enhanced performance of Sb2S3/doped-carbon composites as potential anode materials for sodium-ion batteries: A density functional theory approach, Int. J. Quantum Chem 121 (2021) e26779.
[28] D. Chen, Y. Zhu, S. Han, L. Anatoly, M. Andrey, L. Lu, Investigate the effect of a parallel-cylindrical flow field on the solid oxide fuel cell stack performance by 3D multiphysics simulating, J. Storage Mater. 60 (2023), 106587.
[29] Y. Liu, J. Qin, L. Lu, J. Xu, X. Su, Enhanced microwave absorption property of silver decorated biomass ordered porous carbon composite materials with frequency selective surface incorporation, Int. J. Miner. Metall. Mater. 30 (2023) 525–535.
[30] H. Li, Y. Wang, F. Jiang, M. Li, Z. Xu, A dual-function [Ru (bpy) 3] 2+ encapsulated metal organic framework for ratiometric Al 3+ detection and anticounterfeiting application, Dalton Trans. 52 (2023) 3846–3854.
[31] S. Xu, L. Cai, P. Niu, Z. Li, L. Wei, G. Yao, C. Wang, F. Zheng, Q. Chen, The creation of extra storage capacity in nitrogen-doped porous carbon as high-stable potassium-ion battery anodes, Carbon 178 (2021) 256–264.
[32] J. Yu, X. Li, Y. Shu, L. Ma, X. Zhang, Y. Ding, Anchoring polysulfides in hierarchical porous carbon aerogel via electric-field-responsive switch for lithium sulfur battery, Electrochim. Acta 293 (2019) 458–465.
[33] S. Chen, L. Zhao, J. Ma, Y. Wang, L. Dai, J. Zhang, Edge-doping modulation of N, P-Codoped Porous Carbon Spheres for High-Performance Rechargeable Zn-Air Batteries, Nano Energy 60 (2019) 536–544.
[34] L. Zhao, H. Yang, F. He, Y. Yao, R. Xu, L. Wang, L. He, H. Zhang, S. Li, F. Huang, Biomimetic N-doped sea-urchin-structured porous carbon for the anode material of high-energy-density potassium-ion batteries, Electrochim. Acta 388 (2021), 138565.
[35] B. Ji, F. Zhang, X. Song, Y. Tang, A novel potassium-ion-based dual-ion battery, Adv. Mater. 29 (2017) 1700519.
[36] X. Yang, K. Liu, X. Han, J. Xu, M. Bian, D. Zheng, H. Xie, Y. Zhang, X. Yang, Transformation of waste battery cathode material LiMn2O4 into efficient ultra-low temperature NH3-SCR catalyst: Proton exchange synergistic vanadium modification, J. Hazard. Mater. 459 (2023), 132209.
[37] X. Feng, L. Sun, W. Wang, Y. Zhao, J.-W. Shi, Construction of CdS@ ZnO core–shell nanorod arrays by atomic layer deposition for efficient photoelectrochemical H2 evolution, Sep. Purif. Technol. 324 (2023), 124520.
[38] A.K. Geim, K.S. Novoselov, The rise of graphene, Nat. Mater. 6 (2007) 183–191.
[39] A. Pakdel, C. Zhi, Y. Bando, D. Golberg, Low-dimensional boron nitride nanomaterials, Mater. Today 15 (2012) 256–265.
[40] G. Bhimanapati, N. Glavin, J.A. Robinson, 2D boron nitride: synthesis and applications, in, Semiconductors and Semimetals, Elsevier (2016) 101–147.
[41] I. Muhammad, A. Ali, L. Zhou, W. Zhang, P.K.J. Wong, Vacancy-engineered half-metallicity and magnetic anisotropy in CrSI semiconductor monolayer, J. Alloy. Compd. 909 (2022), 164797.
[42] L. Wang, Y. Jiang, S.-Y. Li, X.-H. Chen, F.-S. Xi, X.-H. Wan, W.-H. Ma, R. Deng, Scalable synthesis of N-doped Si/G@ voids@ C with porous structures for high-performance anode of lithium-ion batteries, Rare Met. (2023) 1–12.
[43] P. Xu, Q. Yuan, W. Ji, R. Yu, F. Wang, N. Huo, Study on the annealing phase transformation mechanism and electrochemical properties of carbon submicron fibers loaded with cobalt, Mater. Express 12 (2022) 1493–1501.
[44] S. Grimme, Accurate description of van der Waals complexes by density functional theory including empirical corrections, J. Comput. Chem. 25 (2004) 1463–1473.
[45] K. Adhikari, A.K. Ray, Carbon- and silicon-capped silicon carbide nanotubes: An ab initio study, Phys Lett Sect A Gen at Solid State Phys 375 (2011) 1817–1823.
[46] A.A. Peyghan, M.B. Tabar, S. Yourdkhani, A theoretical study of OH and OCH<inf>3</inf> free radical adsorption on a nanosized tube of BC<inf>2</inf>N, J. Cluster Sci. 24 (2013) 1–10.
[47] J. Du, X. Sun, G. Jiang, Structures, chemical bonding, magnetisms of small Al-doped zirconium clusters, Phys Lett Sect A Gen at Solid State Phys 374 (2010) 854–860.
[48] X. Liu, B. Zhu, Y. Gao, Structure stability of TiAu4 nanocluster with water adsorption, Phys Lett Sect A Gen at Solid State Phys 380 (2016) 1971–1975.
[49] S. Bashiri, E. Vessally, A. Bekhradnia, A. Hosseinian, L. Edjlali, Utility of extrinsic [60] fullerenes as work function type sensors for amphetamine drug detection: DFT studies, Vacuum 136 (2017) 156–162.
[50] M.W. Schmidt, K.K. Baldridge, J.A. Boatz, S.T. Elbert, M.S. Gordon, J.H. Jensen, S. Koseki, N. Matsunaga, K.A. Nguyen, S. Su, T.L. Windus, M. Dupuis, J. A. Montgomery Jr., General atomic and molecular electronic structure system, J. Comput. Chem. 14 (1993) 1347–1363.
[51] W. Tang, E. Sanville, G. Henkelman, A grid-based Bader analysis algorithm without lattice bias, J. Phys. Condens. Matter 21 (2009), 084204.
[52] G. Henkelman, B.P. Uberuaga, H. Jónsson, A climbing image nudged elastic band method for finding saddle points and minimum energy paths, J. Chem. Phys. 113 (2000) 9901–9904.
[53] Z. Zhao, T. Yu, S. Zhang, H. Xu, G. Yang, Y. Liu, Metallic P 3 C monolayer as anode for sodium-ion batteries, J. Mater. Chem. A 7 (2019) 405–411.
[54] C. Zhang, M. Yu, G. Anderson, R.R. Dharmasena, G. Sumanasekera, The prospects of phosphorene as an anode material for high-performance lithium-ion batteries: a fundamental study, Nanotechnology 28 (2017), 075401.
[55] C. Li, L. He, X. Li, J. Luo, X. Zhu, Z. Chen, M. Xu, Low in-plane atomic density phosphorene anodes for lithium-/sodium-ion batteries, J. Mater. Chem. C 9 (2021) 6802–6814.
[56] S. Mukherjee, L. Kavalsky, C.V. Singh, Ultrahigh Storage and Fast Diffusion of Na and K in Blue Phosphorene Anodes, ACS Appl. Mater. Interfaces 10 (2018) 8630–8639.
[57] L. Li, X. Yu, X. Yang, Y. Fang, X. Zhang, X. Xu, P. Jin, C. Tang, Porous BN with vacancy defects for selective removal of CO from H 2 feed gas in hydrogen fuel cells: a DFT study, J. Mater. Chem. A 4 (2016) 15631–15637.
[58] H. Zhang, C.-J. Tong, Y. Zhang, Y.-N. Zhang, L.-M. Liu, Porous BN for hydrogen generation and storage, J. Mater. Chem. A 3 (2015) 9632–9637.
[59] J.-X. Zhao, H.-X. Wang, Y.-J. Liu, Q.-H. Cai, X.-Z. Wang, Catalyst-free achieving of controllable carbon doping of boron nitride nanosheets by CO molecules: a theoretical prediction, RSC Adv. 3 (2013) 4917–4926.
[60] H. Yin, H. Lin, Y. Zhang, S. Huang, Iron (II) Phthalocyanine Adsorbed on Defective Graphenes: A Density Functional Study, ACS Omega 7 (2022) 43915–43922.
[61] A. Savin, R. Nesper, S. Wengert, T.F. Fässler, ELF: The electron localization function, Angew. Chem. Int. Ed. Eng. 36 (1997) 1808–1832.
[62] G. Henkelman, H. Jónsson, Improved tangent estimate in the nudged elastic band method for finding minimum energy paths and saddle points, J. Chem. Phys. 113 (2000) 9978–9985.
[63] M.I. Khan, G. Nadeem, A. Majid, M. Shakil, A DFT study of bismuthene as anode material for alkali-metal (Li/Na/K)-ion batteries, Mater. Sci. Eng. B 266 (2021), 115061.
[64] S. Chen, F. Zheng, J. Feng, H. Dong, Y. Li, Theoretical study on single-side fluorinated graphene for lithium storage, Appl. Surf. Sci. 560 (2021), 150033.
[65] S. Shi, J. Gao, Y. Liu, Y. Zhao, Q. Wu, W. Ju, C. Ouyang, R. Xiao, Multi-scale computation methods: Their applications in lithium-ion battery research and development, Chin. Phys. B 25 (2015), 018212.
[66] M. Aydinol, A. Kohan, G. Ceder, K. Cho, J. Joannopoulos, Ab initio study of lithium intercalation in metal oxides and metal dichalcogenides, Phys. Rev. B 56 (1997) 1354.
[67] J. Liu, S. Wang, Q. Sun, All-carbon-based porous topological semimetal for Li-ion battery anode material, Proc. Natl. Acad. Sci., 114 (2017) 651–656.